

 Open access • Journal Article • DOI:10.1121/1.2730741

## Numerical investigation of elastic modes of propagation in helical waveguides

— [Source link](#) 





Fabien Treyssède

**Published on:** 01 Jun 2007 - Journal of the Acoustical Society of America (Acoustical Society of America)

**Topics:** Finite element method, Timoshenko beam theory, Guided wave testing, Cylinder and Coordinate system

Related papers:

- [Elastic waves in helical waveguides](#)
- [Finite element prediction of wave motion in structural waveguides.](#)
- [Investigation of elastic modes propagating in multi-wire helical waveguides](#)
- [Guided wave dispersion curves for a bar with an arbitrary cross-section, a rod and rail example](#)
- [Effects of tensile loading on the properties of elastic-wave propagation in a strand](#)

Share this paper:    

View more about this paper here: <https://typeset.io/papers/numerical-investigation-of-elastic-modes-of-propagation-in-82n4uu4whp>



**HAL**  
open science

# A numerical investigation of elastic modes of propagation in helical waveguides

Fabien Treyssède

► **To cite this version:**

Fabien Treyssède. A numerical investigation of elastic modes of propagation in helical waveguides. Journal of the Acoustical Society of America, Acoustical Society of America, 2007, 121, pp.3398-3408. hal-01067643

**HAL Id: hal-01067643**

**<https://hal.archives-ouvertes.fr/hal-01067643>**

Submitted on 23 Sep 2014

**HAL** is a multi-disciplinary open access archive for the deposit and dissemination of scientific research documents, whether they are published or not. The documents may come from teaching and research institutions in France or abroad, or from public or private research centers.

L'archive ouverte pluridisciplinaire **HAL**, est destinée au dépôt et à la diffusion de documents scientifiques de niveau recherche, publiés ou non, émanant des établissements d'enseignement et de recherche français ou étrangers, des laboratoires publics ou privés.

# **A numerical investigation of elastic modes of propagation in helical waveguides**

Fabien Treyssède<sup>a)</sup>

Laboratoire Central des Ponts et Chaussées

Division for Metrology and Instrumentation

Route de Pornic, BP 4129, 44341 Bouguenais Cedex, FRANCE

Received:

Suggested running title: “Elastic propagation modes in helical waveguides”

---

<sup>a)</sup>Electronic mail: [fabien.treysede@lpc.fr](mailto:fabien.treysede@lpc.fr)

**Abstract:**

Steel multi-wire cables are widely employed in civil engineering. They are usually made of a straight core and one layer of helical wires. In order to detect material degradation, non-destructive evaluation methods based on ultrasonics are one of the most promising techniques. However, their use is complicated by the lack of accurate cable models. As a first step, the goal of this paper is to propose a numerical method for the study of elastic guided waves inside a single helical wire. A finite element (FE) technique is used based on the theory of wave propagation inside periodic structures. This method avoids the tedious writing of equilibrium equations in a curvilinear coordinate system yielding translational invariance along the helix centerline. Besides, no specific programming is needed inside a conventional FE code because it can be implemented as a post-processing step of stiffness, mass and damping matrices. The convergence and accuracy of the proposed method are assessed by comparing FE results with Pochhammer-Chree solutions for the infinite isotropic cylinder. Dispersion curves for a typical helical waveguide are then obtained. In the low-frequency range, results are validated with a helical Timoshenko beam model. Some significant differences with the cylinder are observed.

PACS numbers: 43.35.-c, 43.20.Bi, 43.20.Mv, 43.35.Cg

## I. INTRODUCTION **Equation Section 1**

In civil engineering, steel multi-wire cables are widely employed as load-carrying members for many applications such as prestressed structures and bridges. The basic element of these cables, which can be exposed or embedded in concrete, is usually a simple straight strand made of a straight core and one layer of helical wires. The work presented in this paper is limited to exposed cables.

Mainly because of corrosion, material degradation of steel may result in fractures of wires<sup>1,2</sup>, which can lead to the collapse of the overall civil structure. Therefore, a structural health monitoring approach based on non-destructive evaluation methods is strongly needed in order to prevent or detect such failures or for determining the extent of degradation. Ultrasonics is one of the most popular techniques. It consists in analyzing the propagation of elastic guided waves, which are known to be multimodal and dispersive: many propagation modes can propagate simultaneously with propagation velocities depending on frequency. For a better physical understanding of these complex effects – and thus for improving the efficiency of ultrasonic methods – some theoretical models are often required.

The simplest approximating geometry of a multi-wire cable is that of an infinite cylinder. Since the early works of Pochhammer in 1876 and Chree in 1889, wave propagation inside cylindrical elastic waveguides has been widely investigated,

theoretically, numerically and experimentally. Papers on this subject are numerous. For instance, we can cite the paper of Zemanek<sup>3</sup>, who was one of the first authors to present a complete analytical and experimental investigation.

However, some recent experimental studies of multi-wire strands have been realized pointing out the fact that the Pochhammer-Chree dispersion curves cannot accurately predict propagation inside multi-wire strands<sup>4,5,6,7,2</sup>. In fact, the theoretical understanding of guided ultrasonic waves in multi-wire strands is complicated by the helical geometry of peripheral wires, the inter-wire coupling and contact effects, and the presence of applied loads<sup>4,5,6,7,8</sup>.

As a first step toward an increasing complexity, the goal of this paper is to address the first above complicating effect, by proposing a numerical method allowing the study of elastic guided waves inside a single helical wire. To the author knowledge, no such model is yet available in the literature.

In order to deal with complex geometry, some of the most popular and efficient numerical techniques are based on finite element (FE) methods. The so-called semi-analytical finite element (SAFE) method is a first approach that has been used to study uniform waveguides of arbitrary cross-section – see for instance Refs. 9,10,11,12,13,14. Assuming an exponential dependence of the form  $e^{i(kz-\omega t)}$  (where  $k$  is the wavenumber,  $z$  the axis waveguide, and  $\omega$  is the frequency), SAFE methods are interesting from a

computational point of view because only the cross-section has to be meshed, hence drastically reducing the number of degrees of freedom (dofs). A drawback of these methods is that they require some specific programming inside a FE code. This can be circumvented by an interesting alternative proposed by Wilcox et al.<sup>15</sup> based on the use of an axisymmetric harmonic approach, which allows the study of straight waveguides (of arbitrarily large radius) as well as toroidal structures<sup>16</sup>. However, only a limited number of real wavenumbers can be considered with this procedure (in particular, modes with imaginary or complex wavenumbers cannot be dealt with).

A second approach is based on the theory of wave propagation in periodic structures. From Floquet's principle, this theory allows to study the single repetitive substructure alone, thanks to the application of a set of periodic boundary conditions involving a propagation constant corresponding to the eigenvalue. A review on the topic can be found in Ref. 17. Based on a general theory presented by Mead<sup>18</sup>, some periodic FE approaches and procedures have then been developed – see for instance Refs. 19,20,21,22. These methods are more general than SAFE's because non-uniform waveguides can be analyzed (propagation constants can be considered as the non-uniform waveguides generalization of axial wavenumbers in uniform waveguides). Similarly to SAFE methods, periodic FE approaches only need the mesh of one repetitive cell, which tremendously reduces the computational cost. Besides, they can be implemented as a post-process step of a standard FE code providing stiffness, mass and damping matrices.

For modeling a single helical wire, which is a uniform waveguide, both SAFE and periodic FE approaches can be applied. However, the use of SAFE methods would a priori raise some calculation and programming difficulties. First, the elasticity equilibrium equations should be written in a helical curvilinear coordinate system, usually non-orthogonal, yielding a translational invariance along the helix centerline. Second, solving the obtained equations would require a complete re-programming inside a standard FE code (that typically uses a cartesian or a cylindrical coordinate system).

In this paper, the numerical technique developed is based on a periodic FE approach. It uses the outputs of a conventional FE code, that are the stiffness, mass and damping matrices. In Sec. II, the equilibrium equations and some FE procedures are first recalled. Unlike Refs. 21 and 22, the considered final eigensystem involves interior dofs, which may avoid some costly matrix inversion. A three-dimensional mapping yielding a translational invariance is then proposed in Sec. III. Based on this mapping, a peculiar mesh is generated, and the left and right dofs are transformed into their curvilinear counterparts. Numerical results are given in Sec. IV. The method is first validated with the Pochhammer-Chree solution. The numerical accuracy and convergence of the proposed numerical method is also briefly studied. Computations for a single helical wire are then realized with characteristics typically encountered in civil engineering. In the low frequency range, the results are validated by comparing those obtained from a



one-dimensional Timoshenko helical beam. Section V finally gives some general conclusions.

## II. FINITE ELEMENT MODELING OF PERIODIC ELASTIC WAVEGUIDES

Waveguides can be considered as periodic systems. Because we are only interested in one-dimensional waveguides in this paper, the unit periodic cells are only connected end-to-end (but with multiple dofs coupling between them). This section describes the FE approach for one-dimensional periodic systems.

### A. Equilibrium equations

Assuming a linearly elastic material, small strains and displacements and a time harmonic  $e^{-i\omega t}$  dependence, the governing equilibrium equations are given by:

$$\nabla \cdot \boldsymbol{\sigma} + \rho \omega^2 \mathbf{u} = \mathbf{0} \quad \text{in } \Omega \quad (1)$$

$\mathbf{u}$  and  $\boldsymbol{\sigma}$  respectively denote the displacement vector field and the Cauchy stress tensor.  $\rho$  is the material density and  $\Omega$  represents the domain occupied by one periodic cell (or an integer-multiple) constituting the overall infinite periodic structure. Let us denote by  $L$  the axial length of this cell. Of course, there is no external body force for the purpose of studying propagation modes. The stress-strain and strain-displacement relations are respectively given by  $\boldsymbol{\sigma} = \mathbf{C} : \boldsymbol{\varepsilon}$  and  $\boldsymbol{\varepsilon} = 1/2(\nabla \mathbf{u} + \nabla \mathbf{u}^T)$ .

$\Gamma_{ext}$ ,  $\Gamma_L$  and  $\Gamma_R$  are respectively the external boundary, the left cross-section boundary and the right cross-section boundary of the waveguide periodic cell ( $\partial\Omega = \Gamma_{ext} \cup \Gamma_L \cup \Gamma_R$ ), as shown in Fig. 1. A typical waveguide may be subjected to some traction-free or zero-displacement boundary conditions on its external boundary:

$$\boldsymbol{\sigma} \cdot \mathbf{n} = \mathbf{0} \quad \text{or} \quad \mathbf{u} = \mathbf{0} \quad \text{on } \Gamma_{ext} \quad (2)$$

From Floquet's theorem and as defined by Mead<sup>18</sup>, free wave motion through an infinite periodic system occurs when there is no external force and is characterized by the displacements in one element being equal to the corresponding displacements in the adjacent element times a factor denoted  $\lambda$  (to be found). Hence from displacement and stress continuities, the following periodic boundary conditions hold (see for instance Ref. 23):

$$\boldsymbol{\sigma} \cdot \mathbf{n}|_{\Gamma_R} = -\lambda \boldsymbol{\sigma} \cdot \mathbf{n}|_{\Gamma_L} \quad \text{and} \quad \mathbf{u}|_{\Gamma_R} = \lambda \mathbf{u}|_{\Gamma_L} \quad (3)$$

$\mathbf{n}$  is the outer unit normal from the subsystem  $\Omega$ . Setting  $\lambda = e^{ikL}$ ,  $ikL$  is often called the axial propagation constant.  $k$  then corresponds to the axial wavenumber. The real and imaginary parts of  $kL$  respectively govern the phase change and the attenuation (or growth) over a periodic cell.  $\text{Re}kL$  can only be determined up to  $2m\pi$ , and as noticed in Ref. 19, only the principal value of the phase constant is calculated (i.e.  $-\pi < \text{Re}kL < \pi$ ). It should be noted that some more general periodic boundary conditions than Eqs. (3) may be found in Ref. 23, taking into account the presence of some additional connecting structures (periodic supports or stiffeners for instance).

Without loss of generality in this paper, we will only consider waveguides having free external boundaries and no additional connecting structures.

## B. Finite element method

Applying a conventional FE analysis, the discretized equations of motion (1) become after applying boundary conditions (2):

$$(\mathbf{K} - i\omega\mathbf{C} + \omega^2\mathbf{M})\mathbf{u} = \mathbf{f} \quad (4)$$

where  $\mathbf{K}$ ,  $\mathbf{M}$  and  $\mathbf{C}$  are the stiffness, mass and damping symmetric matrices.  $\mathbf{u}$  and  $\mathbf{f}$  are respectively the vector of nodal dofs (usually the nodal displacements) and the vector of nodal forces. It should be outlined that the stiffness matrix  $\mathbf{K}$  might be complex when the presence of viscoelastic damping, if any, is modeled through the use of complex material properties. Depending on the damping model used, such properties can also be frequency dependent. Besides, the matrix  $\mathbf{C}$  corresponding to viscous damping should be zero here because this kind of damping model has been implicitly neglected in Eq. (1) (without loss of generality for the proposed FE method).  $\mathbf{u}$  may be partitioned into dofs associated with the left ( $L$ ) and right ( $R$ ) cross-section nodes, and with the interior ( $I$ ) nodes, yielding the following system:

$$\begin{bmatrix} \mathbf{D}_{LI} & \mathbf{D}_{LL} & \mathbf{D}_{LR} \\ \mathbf{D}_{II} & \mathbf{D}_{IL} & \mathbf{D}_{IR} \\ \mathbf{D}_{RI} & \mathbf{D}_{RL} & \mathbf{D}_{RR} \end{bmatrix} \begin{Bmatrix} \mathbf{u}_L \\ \mathbf{u}_I \\ \mathbf{u}_R \end{Bmatrix} = \begin{Bmatrix} \mathbf{f}_L \\ \mathbf{0} \\ \mathbf{f}_R \end{Bmatrix} \quad (5)$$

where we have introduced the dynamic stiffness matrix  $\mathbf{D} = \mathbf{K} - i\omega\mathbf{C} + \omega^2\mathbf{M}$  from Eq. (4).

In addition, the discretized periodic condition (3) becomes:

$$\mathbf{u}_R = \lambda \mathbf{u}_L \quad \text{and} \quad \mathbf{f}_R = -\lambda \mathbf{f}_L \quad (6)$$

Applying (6) into (5) and solving for  $\mathbf{f}_R$ , Eq. (5) becomes:

$$\left( \mathbf{D}_1 + \lambda \mathbf{D}_2 + \frac{1}{\lambda} \mathbf{D}_3 \right) \mathbf{q} = \mathbf{0} \quad (7)$$

with the notations:

$$\mathbf{D}_1 = \begin{bmatrix} \mathbf{D}_{LL} + \mathbf{D}_{RR} & \mathbf{D}_{LI} \\ \mathbf{D}_{IL} & \mathbf{D}_{II} \end{bmatrix}, \quad \mathbf{D}_2 = \begin{bmatrix} \mathbf{D}_{LR} & \mathbf{0} \\ \mathbf{D}_{IR} & \mathbf{0} \end{bmatrix}, \quad \mathbf{D}_3 = \begin{bmatrix} \mathbf{D}_{RL} & \mathbf{D}_{RI} \\ \mathbf{0} & \mathbf{0} \end{bmatrix}, \quad \mathbf{q} = \begin{Bmatrix} \mathbf{u}_L \\ \mathbf{u}_I \end{Bmatrix} \quad (8)$$

The above system is a quadratic eigenvalue problem to be solved for  $\lambda$ .

Because of the symmetry of  $\mathbf{D}$  (yielding  $\mathbf{D}_1^T = \mathbf{D}_1$  and  $\mathbf{D}_2^T = \mathbf{D}_3$ ) and using the property  $\det \mathbf{A}^T = \det \mathbf{A}$  ( $\mathbf{A}$  is any matrix), it can easily be checked that if  $\lambda$  is an eigenvalue of (7), then  $1/\lambda$  is also an eigenvalue. Hence, the eigenproblem has two sets of eigensolutions  $(\lambda_j, \boldsymbol{\varphi}_j^+)$  and  $(1/\lambda_j, \boldsymbol{\varphi}_j^-)$  ( $j=1, \dots, n$ ), representing  $n$  positive-going and  $n$  negative-going wave types. As proved by Mead<sup>18</sup>,  $n$  is the minimum number of coupling dofs obtainable by appropriate choice of the junction between cells. In the absence of damping, eigenvalues for which  $|\lambda_j|=1$  (i.e.  $k$  real) represent freely propagating waves and those for which  $\lambda_j$  is real (i.e.  $k$  imaginary) represent evanescent waves. The other eigenvalues (for which  $k$  is complex) represent decaying but oscillatory waves.

The eigenproblem (7) may be first recast into a generalized linear eigensystem (see Eqs. (9) or (10) for instance) and then solved using some standard numerical solvers. However, it may lead to ill-conditioning due to the fact that it has both very large and small eigenvalues  $\lambda$  and  $1/\lambda$  (such eigenvalues represent some rapidly decaying waves). This typically happens when the number of dofs is not small any more, as for two-dimensional sections (even if interior dofs are eliminated<sup>21</sup>). In order to overcome these difficulties, a reformulation of the eigensystem in terms of  $(\lambda + 1/\lambda)$  has been proposed by some authors<sup>24,20,21</sup>.

Then, following the same procedure as in Ref. 21, the system (7) is first recast into both following equivalent forms of linear eigenproblem:

$$\left( \begin{bmatrix} -\mathbf{D}_3 & -\mathbf{D}_1 \\ \mathbf{0} & -\mathbf{D}_3 \end{bmatrix} - \lambda \begin{bmatrix} \mathbf{0} & \mathbf{D}_2 \\ -\mathbf{D}_3 & \mathbf{0} \end{bmatrix} \right) \begin{Bmatrix} \mathbf{q} \\ \lambda \mathbf{q} \end{Bmatrix} = \begin{Bmatrix} \mathbf{0} \\ \mathbf{0} \end{Bmatrix} \quad (9)$$

and:

$$\left( \begin{bmatrix} \mathbf{D}_2 & \mathbf{0} \\ \mathbf{D}_1 & \mathbf{D}_2 \end{bmatrix} - \frac{1}{\lambda} \begin{bmatrix} \mathbf{0} & \mathbf{D}_2 \\ -\mathbf{D}_3 & \mathbf{0} \end{bmatrix} \right) \begin{Bmatrix} \mathbf{q} \\ \lambda \mathbf{q} \end{Bmatrix} = \begin{Bmatrix} \mathbf{0} \\ \mathbf{0} \end{Bmatrix} \quad (10)$$

The sum of Eqs. (9) and (10) yields after some rearrangements an eigenproblem written in terms of  $(\lambda + 1/\lambda)$  only:

$$\left( \begin{bmatrix} -\mathbf{D}_1 & \mathbf{D}_3 - \mathbf{D}_2 \\ \mathbf{D}_2 - \mathbf{D}_3 & -\mathbf{D}_1 \end{bmatrix} - \left( \lambda + \frac{1}{\lambda} \right) \begin{bmatrix} \mathbf{D}_3 & \mathbf{0} \\ \mathbf{0} & \mathbf{D}_2 \end{bmatrix} \right) \begin{Bmatrix} \mathbf{q} \\ \lambda \mathbf{q} \end{Bmatrix} = \begin{Bmatrix} \mathbf{0} \\ \mathbf{0} \end{Bmatrix} \quad (11)$$

Note that the eigensystems (9)–(11) are all unsymmetric. Now, the eigenvalues of (11) occur in pairs of equal values  $(\lambda_j + 1/\lambda_j)$ . The associated eigenvectors, denoted as  $\Phi'_j$  and  $\Phi''_j$ , correspond with a linear combination of the original eigenvectors, denoted as  $\Phi_j^+$  and  $\Phi_j^-$ , associated with  $\lambda_j$  and  $1/\lambda_j$  and obtained from (9) (or (10)). This linear combination is arbitrarily obtained in a computer code. For restoring the original eigenvectors, we proceed as in Ref. 20. First, we expand the original eigenvectors as  $\Phi_j = \alpha_1 \Phi'_j + \alpha_2 \Phi''_j$  (the superscripts + and – have been dropped for simplicity). Introducing this expansion into Eq. (9) (for instance), and left-multiplying by  $\Phi_j'^T$ , we get the following relation between  $\alpha_1$  and  $\alpha_2$ :

$$\alpha_2 = -\frac{\Phi_j'^T \mathbf{A}_\lambda \Phi'_j}{\Phi_j'^T \mathbf{A}_\lambda \Phi''_j} \alpha_1 \quad \text{with } \mathbf{A}_\lambda \square \begin{bmatrix} -\mathbf{D}_3 & -\mathbf{D}_1 \\ \mathbf{0} & -\mathbf{D}_3 \end{bmatrix} - \lambda \begin{bmatrix} \mathbf{0} & \mathbf{D}_2 \\ -\mathbf{D}_3 & \mathbf{0} \end{bmatrix} \quad (12)$$

The constant  $\alpha_1$  is finally obtained by normalizing eigenvectors. From the computed eigenvalues, the axial wavenumbers are given up to  $2m\pi$  by:

$$k_j^\pm L = \pm \cos^{-1} \left\{ \frac{1}{2} (\lambda_j + 1/\lambda_j) \right\} + 2m\pi \quad (13)$$

It has to be noted that the interior dofs  $\mathbf{u}_l$  could have been condensed out in Eqs. (7)–(11), as usually done in the literature when using a transfer matrix approach<sup>20,21,22,24</sup>. However, it would have required the computation of the inverse of  $\mathbf{D}_{II}$ . This can be costly from a numerical point of view when the number of interior dofs becomes large, which may indeed be the case in this paper.

### III. REQUIREMENTS FOR HELICAL WAVEGUIDES

The three-dimensional cell domain is meshed using standard FE. Nevertheless, the mesh must satisfy a compatibility constraint between the left-section and the right-section: each dof of the right section must be related to a corresponding dof of the left section chosen in such a way that the periodic conditions (6) hold. This implies that the two dimensional meshing of the right section must be compatible with that of the left section and that the ordering of left and right dofs must be carefully considered.

For instance, for an infinite isotropic cylindrical straight waveguide, the mesh of the right section must simply be a translation of the left section mesh along the cylinder axis. Because of the obvious geometrical translational invariance along that axis, the axial length of a periodic cell can be arbitrarily small (typically one element length).

At first sight, the unit periodic cell of a helical waveguide should have a length that equals to the helix step, denoted as  $L_0$  below. Nevertheless, such a length would require a three-dimensional mesh involving a large number of dofs in practice. Fortunately, as shown in the following, the length of this unit periodic cell can be arbitrarily reduced by considering a specific mapping yielding a translational invariance along the helix centerline.

The helix centerline curve can be described by the following position vector:

$$\mathbf{R}(s) = R_0 \cos\left(\frac{2\pi}{l_0}s\right)\mathbf{e}_x + R_0 \sin\left(\frac{2\pi}{l_0}s\right)\mathbf{e}_y + \frac{L_0}{l_0}s\mathbf{e}_z \quad (14)$$

where  $l_0 = (L_0^2 + 4\pi^2 R_0^2)^{1/2}$ .  $(\mathbf{e}_x, \mathbf{e}_y, \mathbf{e}_z)$  denotes the cartesian orthonormal basis.  $R_0$  and  $L_0$  are respectively the radius of the centerline in the  $(x,y)$  plane and the helix step along the  $z$  axis. A complete period can thus be described by the parameter  $s$  varying from 0 to  $l_0$ . It should be noted that the parameter  $s$  has been chosen so that it corresponds to the arc length (hence,  $l_0$  is the curvilinear length of one helix step). The unit tangent vector to the centerline is then directly given by  $\mathbf{T} = d\mathbf{R}/ds$ . The unit normal can be defined from the Serret-Frenet formulae  $d\mathbf{T}/ds = \kappa_0\mathbf{N}$ , and the unit binormal vector is  $\mathbf{B} = \mathbf{T} \wedge \mathbf{N}$  (the following Serret-Frenet formulae also holds:  $d\mathbf{N}/ds = \tau_0\mathbf{B} - \kappa_0\mathbf{T}$ ,  $d\mathbf{B}/ds = -\tau_0\mathbf{N}$ ). For the curve defined by (14), both the curvature  $\kappa_0$  and the tortuosity  $\tau_0$  are constant:  $\kappa_0 = 4\pi^2 R_0/l_0^2$  and  $\tau_0 = 2\pi L_0/l_0^2$ .

Now, a new coordinate system is constructed from the orthonormal basis  $(\mathbf{T}, \mathbf{N}, \mathbf{B})$ , for which any Cartesian vector  $\mathbf{x}$  can be expressed as:

$$\mathbf{x}(u, v, s) = \mathbf{R}(s) + \alpha\mathbf{N}(s) + \beta\mathbf{B}(s) \quad (15)$$

The so defined coordinates  $(\alpha, \beta, s)$  are single valued only if  $\alpha$  and  $\beta$  are small enough on the cross-section (this restriction will be implied in the remaining). Using the above Serret-Frenet formulae, it can be shown that this kind of mapping yields a non-



orthogonal covariant basis  $(\partial\mathbf{x}/\partial\alpha, \partial\mathbf{x}/\partial\beta, \partial\mathbf{x}/\partial s)$ , denoted by  $(\mathbf{g}_1, \mathbf{g}_2, \mathbf{g}_3)$ . The metric tensor of such a mapping, defined by  $g_{mn} = \mathbf{g}_m \cdot \mathbf{g}_n$ , is given by:

$$\mathbf{g} = \begin{bmatrix} 1 & 0 & -\tau_0\beta \\ 0 & 1 & \tau_0\alpha \\ -\tau_0\beta & \tau_0\alpha & \tau_0^2(\alpha^2 + \beta^2) + (1 - \kappa_0\alpha)^2 \end{bmatrix} \quad (16)$$

Consequently,  $\mathbf{g}$  does not depend on the third curvilinear coordinate  $s$  (for a helix,  $\kappa_0$  and  $\tau_0$  are constant). Provided that the cross-section of the waveguide does not vary along  $s$  (nor the material properties), this means that this curvilinear coordinate system yields a translational invariance along  $s$ .

To be more precise, this transformation allows the investigation of the propagation modes because  $s$  would not appear explicitly in the equilibrium equations written in the curvilinear system, except for derivatives with respect to  $s$ . Hence, an exponential  $e^{iks}$  might be separated from all field component, and  $\partial/\partial s$  replaced by  $ik$ . In other terms, a Fourier transform in the  $s$  direction can be performed so that we can still speak of propagation modes. It has to be pointed out that similar kinds of the above helical mapping had already been considered in electromagnetics to study helical waveguides, analytically<sup>25</sup> or numerically<sup>26</sup>.

In this paper, we are interested in solving the equilibrium equations through a periodic FE modeling. This avoids the writing of equilibrium equations in the above

curvilinear coordinates, which would be very tedious and would also require some specific programming inside a FE code.

With the proposed method instead, what must be done is relating the right section nodes of the three-dimensional mesh to the left section nodes through the mapping defined by (15). And as a consequence of the translational invariance along  $s$ , the length of one unit periodic cell may be arbitrarily small as for the cylinder case. Besides, in order for the translational invariance along  $s$  to hold, the left and right dofs involved in Eqs. (6) must be the components in the curvilinear basis. However, the outputs of a conventional FE code are usually the cartesian  $(x, y, z)$  components of the nodal displacement and force, and thus need to be transformed into the curvilinear  $(\alpha, \beta, s)$  components through the Jacobian matrix, as follows:

$$\begin{Bmatrix} u_k^x \\ u_k^y \\ u_k^z \end{Bmatrix} = \mathbf{J}(\alpha_k, \beta_k, s_k) \begin{Bmatrix} u_k^1 \\ u_k^2 \\ u_k^3 \end{Bmatrix}, \quad \begin{Bmatrix} f_k^x \\ f_k^y \\ f_k^z \end{Bmatrix} = \mathbf{J}^{-T}(\alpha_k, \beta_k, s_k) \begin{Bmatrix} f_{1k} \\ f_{2k} \\ f_{3k} \end{Bmatrix} \quad (17)$$

where  $k$  denotes the node number,  $u_k^i$  is the contravariant displacement component with respect to the covariant basis vector  $\mathbf{g}_i$  ( $i=1,2,3$ ).  $\mathbf{J}(\alpha_k, \beta_k, s_k)$  is the covariant Jacobian matrix, whose column  $i$  correspond to the cartesian components of  $\mathbf{g}_i$  evaluated at node  $k$ . From Eq. (15), it can be shown that:

$$\mathbf{J}(\alpha_k, \beta_k, s_k) = \begin{bmatrix} -\cos \frac{2\pi}{l_0} s_k & \frac{L_0}{l_0} \sin \frac{2\pi}{l_0} s_k & \frac{2\pi}{l_0} (\alpha_k - R_0) \sin \frac{2\pi}{l_0} s_k + \tau_0 \beta_k \cos \frac{2\pi}{l_0} s_k \\ -\sin \frac{2\pi}{l_0} s_k & -\frac{L_0}{l_0} \cos \frac{2\pi}{l_0} s_k & -\frac{2\pi}{l_0} (\alpha_k - R_0) \cos \frac{2\pi}{l_0} s_k + \tau_0 \beta_k \sin \frac{2\pi}{l_0} s_k \\ 0 & \frac{2\pi R_0}{l_0} & \frac{L_0}{l_0} \end{bmatrix} \quad (18)$$

From the previous notations,  $\mathbf{J}^{-T}(\alpha_k, \beta_k, s_k)$  corresponds to the contravariant Jacobian matrix and  $f_{ik}$  ( $i=1,2,3$ ) denote the covariant force components with respect to the contravariant basis  $(\mathbf{g}^1, \mathbf{g}^2, \mathbf{g}^3)$ , defined by  $\mathbf{g}^i \cdot \mathbf{g}_j = \delta_j^i$ .

The above matrix (18) may be assembled on the left (resp. right) dofs, yielding a matrix denoted by  $\mathbf{J}_L$  (resp.  $\mathbf{J}_R$ ). The initial cartesian components, denoted by a superscript  $c$ , can be transformed using a global transformation matrix  $\mathbf{Q}$  into  $\mathbf{u}^c = \mathbf{Q}\mathbf{u}$ ,  $\mathbf{f}^c = \mathbf{Q}^{-T}\mathbf{f}$  with the notations:

$$\mathbf{u}^c = \begin{Bmatrix} \mathbf{u}_L^c \\ \mathbf{u}_I^c \\ \mathbf{u}_R^c \end{Bmatrix}, \mathbf{u} = \begin{Bmatrix} \mathbf{u}_L \\ \mathbf{u}_I \\ \mathbf{u}_R \end{Bmatrix}, \mathbf{f}^c = \begin{Bmatrix} \mathbf{f}_L^c \\ \mathbf{f}_I^c \\ \mathbf{f}_R^c \end{Bmatrix}, \mathbf{f} = \begin{Bmatrix} \mathbf{f}_L \\ \mathbf{f}_I \\ \mathbf{f}_R \end{Bmatrix}, \mathbf{Q} = \begin{bmatrix} \mathbf{J}_L & 0 & 0 \\ 0 & \mathbf{I} & 0 \\ 0 & 0 & \mathbf{J}_R \end{bmatrix} \quad (19)$$

Then, before applying the procedures detailed in Sec. IIB, the initial cartesian dynamic system obtained from a standard FE code, denoted  $\mathbf{D}^c \mathbf{u}^c = \mathbf{f}^c$ , must be first transformed into  $\mathbf{D}\mathbf{u} = \mathbf{f}$  where  $\mathbf{D}$  is given by:

$$\mathbf{D} = \mathbf{Q}^T \mathbf{D}^c \mathbf{Q} \quad (20)$$

$\mathbf{D}$  is still symmetric thanks to the transformation choice (17). Note that if contravariant components had also been chosen for forces, unsymmetric dynamic stiffness matrices might result.

#### IV. NUMERICAL RESULTS

In this section, the material is assumed to be isotropic. No structural damping will be considered for simplicity.  $E$  and  $\nu$  will denote the Young's modulus and the Poisson coefficient respectively. For a steel wire, a typical value of  $\nu=0.30$  will be chosen. We consider waveguides with a circular cross-section of radius  $a$ .

##### A. Preliminary numerical considerations

In order to obtain the adequate meshing between the left and right cross-section, the technique used in this paper consists in generating a two-dimensional mesh in the  $(\alpha, \beta)$  plane of the left section (at  $s=s_L$  constant). This mesh is then extruded into a three-dimensional mesh by simply translating each node – with  $(\alpha, \beta)$  held constant – along the centerline  $s$ . The two-dimensional elements used are 3-node triangles, extruded into 6-node prisms.

The eigenproblem (11) is solved using an algorithm based on the generalized Jacobi method. Variables are first adimensionalized with some characteristic length and time, chosen as  $a$  and  $\omega/c_s$  respectively ( $c_s = \sqrt{E/2\rho(1+\nu)}$  is the shear velocity). Hence, the

dimensionless frequency is given by  $\Omega = \omega a / c_s$ . In order to reduce the computational time, some upper and lower bounds can be set for the eigenvalue searching interval. The real value of the computed eigenvalues is given by  $\text{Re}(\lambda + 1/\lambda) = 2 \cos(\text{Re } kL) \cosh(\text{Im } kL)$ . Then, it can be noticed that propagating (resp. evanescent) waves satisfy the inequality  $|\text{Re}(\lambda + 1/\lambda)| < 2$  (resp.  $\geq 2$ ). One is usually interested in the propagating and less attenuated waves, so that the upper and lower bounds can be set to  $\pm 2 \cosh \gamma$  (where  $\gamma$  is a user-defined parameter).

The accuracy of numerical results is independent on the axial number of elements (but it may be dependent on the axial element length as shown further). Hence, only one layer of elements would be enough. This is interesting because in practice, the cell length  $L$  is thus sufficiently small in order to have  $-\pi < \text{Re } k_j^\pm L < \pi$  in Eq. (13), which avoids the undetermination up to  $2m\pi$ . In this paper, two layers have generally been used because a faster convergence was observed with the Arnoldi algorithm used.

## **B. Validation for an infinite isotropic cylinder and accuracy**

The numerical model is first validated with the Pochhammer-Chree semi-analytical model<sup>27,3</sup> describing elastic propagation in an infinite isotropic cylinder (i.e.  $L_0 \rightarrow \infty$ ). FE and analytical axial wavelengths are compared for a given dimensionless frequency  $\Omega = 1$ , for the three lowest real solutions, the first imaginary and the first complex solutions, which respectively corresponds to: the  $L(0,1)$  longitudinal mode, the torsional

mode, the  $F(1,1)$  flexural mode, the  $F(1,2)$  flexural mode (evanescent), and the  $F(2,1$  &  $2)$  mode (inhomogeneous).

In order to assess the convergence and accuracy of the numerical method, FE results have been computed with a sequence of four refined meshes, shown in Fig. 2 with characteristics given in Table I. The successive refinements have been made by dividing each triangle of the previous cross-section mesh into four triangles. Plots of the dispersion error vs. the mesh fineness parameter  $1/h$  are then obtained ( $h$  is chosen as the dimensionless maximum element length). The dispersion error is chosen as the ratio  $|ka - k_{ref}a|/|k_{ref}a|$ , where  $ka$  and  $k_{ref}a$  are respectively the adimensional FE and Pochhammer-Chree axial wavenumbers. Note that only one layer of element has been used, with an axial length of elements equal to  $h$  (as a first choice). Also shown in Table I is the rough criterion given by the ratio  $\lambda_s/h$  (where  $\lambda_s = 2\pi/\Omega$  is the dimensionless shear wavelength), often used in FEM methods to characterize the fineness of a mesh at a given frequency. The Pochhammer-Chree solutions for the  $L(0,1)$ , torsional,  $F(1,1)$ ,  $F(1,2)$  and  $F(2,1$  &  $2)$  modes are respectively  $k_{ref}a = 0.626, 1.000, 1.421, 0.740i, 0.953+1.905i$ .

Figure 3 gives the convergence curve for each mode. It can be observed that the rate of convergence approaches a quadratic behavior for every type of modes. The accuracy for the propagating bending mode is somewhat lower, as well as for the imaginary and complex solutions (corresponding to upper bending modes). As intuitively expected, a

general trend for the accuracy of a given mode is to decrease as its order increases (i.e. as its modeshapes becomes more and more complex). The same behavior has been reported with a SAFE method by Damljjanovic et al.<sup>13</sup>.

With mesh 3, a dispersion error less than 1% is reached for all modes, except for the inhomogeneous one (2%). It can be concluded that a rough criterion of  $\lambda_s/h=25$  is thus quite acceptable, which may be not the case for  $\lambda_s/h=10$ . Note that it coincides well with the criterion proposed for SAFE methods by Galan et al.<sup>28,29</sup> when using 3-node triangles.

In the above results, the axial length of elements, denoted by  $h_{axis}$ , was set to  $h$ . This is the worst element size. By reducing  $h_{axis}$ , dispersion results may be further improve for a given cross-section mesh, as shown in Fig. 4. The mesh used for the cross-section is that of mesh 2, with a criterion  $\lambda_s/h=10$ . By reducing  $h_{axis}$  to  $0.3h$ , the dispersion error becomes less than 1% for all propagating modes, whereas the improvement is weaker for the imaginary and complex solutions. Of course, the element axial length cannot be infinitely reduced due to machine rounding errors ( $0.3h$  was found to be a limit, under which the algorithm used hardly converges).

### C. Dispersion analysis of a typical helical wire

The wave modes propagating inside a peripheral wire constituting a typical seven-wire strand is now numerically studied. The helix radius of such a peripheral wire is

$R_0=2a$ . The helix step is given by  $L_0 = 2\pi R_0 / \tan \phi$ , where  $\phi$  denotes the lay angle of the helix.

In order to make a consistent comparison of wavenumbers with those of a cylindrical wire,  $L$  is not chosen as the axial length along the  $z$ -axis, but as the arc length along the helix centerline of the FE cell.

As a first example, some FE wavenumbers are computed for a helical waveguide having a significant lay angle  $\phi=45^\circ$  and for a given adimensional frequency  $\Omega=0.75$ . In order to demonstrate the validity of the approach, a varying number of layers of elements has been used while keeping the same cross-sectional mesh ( $\lambda_s/h=20$ ,  $h_{axis}=0.7h$ ). Figure 5 exhibits two examples of meshes, used for only one layer and for sixty layers. The sixty layers mesh exactly represents the whole helix step (6771 dofs). Hence, FE results obtained with this mesh should be understood as reference solutions because this mesh is the obvious periodic unit cell, so that the specific mapping described in Sec. III is not needed. These reference solutions are given by the last column of Table II for the propagating modes denoted as  $L(0,1)$ , torsional,  $F(1,1)^-$  and  $F(1,1)^+$  (the notation  $-/+$  is explained further below). For a cylinder, these values are found to be  $ka=0.4669$ ,  $0.7485$ ,  $1.1550$  and  $1.1550$  (with an error less than 1% compared with the Pochhammer-Chree solutions), thus yielding a strong difference with the helical behavior. The important conclusion that can be drawn from Table II is that as expected, results are not dependent upon the axial number of layers and are identical to those obtained with a whole step



mesh. This would not have been the case if the mapping proposed in Sec. III were not translationally invariant. As a side remark, results given by Table II have been corrected when necessary, because of the  $2m\pi$  undetermination of Eq. (13) occurring when  $L$  is large enough.

The remaining of this paper is now devoted to dispersion analysis of helical waveguides having smaller lay angles, more realistic in civil engineering. In the following, two layers of elements have been used. Dispersion curves have been obtained by computing wavenumbers for discrete frequencies. In order to reduce computation time, frequency steps have been only refined near cut-offs, where wavenumbers may be scarce. Note that the method only returns discrete points and does not provide continuous lines representing dispersion curves. The task of joining points together that lie on the same mode has been done by comparing modeshapes between two successive frequencies. Because purely real or imaginary (resp. fully complex) solutions occur in pairs of opposite signs (resp. in quadruples of complex conjugates and opposite signs), only the absolute values of real and imaginary parts are plotted, on the same axis (which is more readable than a three-dimensional plot).

In order to validate the numerical model, the FE results are first compared in the low-frequency range with results obtained from a helical Timoshenko beam model. Such a model was initially proposed by Wittrick<sup>30</sup> in 1966 in order to study analytically the validity of simplified spring models. Wittrick's model is briefly recalled in Appendix, as

well as the numerical method used in this paper to solve it. This mono-dimensional model has twelve eigenvalues, corresponding to six positive and six negative traveling modes.

The lay angle of the helix is set to a common value of  $7.5^\circ$  (for a typical radius  $a=2.5\text{mm}$ , it corresponds to a step  $L_0=23.9\text{cm}$ ). Figure 6 shows the dispersion curves obtained from both models with the adimensional frequency  $\Omega$  varying from 0.02 to 2, and for both the cylindrical and helical geometry. Following the conclusions drawn previously, a rough criterion of  $\lambda_s/h=25$  (at  $\Omega = 2$ ) has been chosen for the mesh, shown in Fig. 7, with  $h_{axis}$  set to  $0.7h$ . 3048 elements and 3564 dofs have been generated.

A very good agreement between both models is obtained in the low frequency range. In the cylinder case, it has been verified that FE results yield an error less than 0.5% for all modes (except for wavenumbers near cutoff because of their high sensitivity to a small frequency variation) compared with the Pochhammer-Chree solution. In order to further assess the convergence of FE results in the helical case, Fig. 8 plots the convergence and accuracy curves for every propagation modes at  $\Omega=2$ , obtained by using four refined meshes (as done in the previous subheading). Because no analytical solution is available for the helical geometry, the reference value has been chosen as the one obtained with the most refined mesh ( $h=0.06$ , corresponding to approximately  $\lambda_s/h=50$ ). The reference adimensional wavenumbers computed for the propagating modes, denoted as  $L(0,1)$ , torsion,  $F(1,1)^-$ ,  $F(1,1)^+$ ,  $F(1,2)^-$  and  $F(1,2)^+$ , are respectively

1.306, 1.999, 2.335, 2.464, 0.394 and 0.523. As observed previously in the cylinder case, the curves exhibit a nearly quadratic rate of convergence, and an error less than 1% for the  $\lambda_s/h=25$  mesh ( $h=0.12$ ).

All the above results tend to demonstrate that a good accuracy is achieved by the helical FE model. Now, from a physical point of view, an interesting feature can be observed by comparing the cylindrical and helical cases. The wavenumbers of the compressional  $L(0,1)$  and the torsional modes are unchanged by the helical geometry (provided that the helix arc length is considered, as stated earlier). This is not the case for flexural modes, which occur in distinct roots instead of double roots because of the lack of symmetry of the helical geometry. A similar phenomenon was observed by Demma et al.<sup>16</sup> for toroidal waveguides when studying bends in pipelines. For simplicity, and though this notation may be somewhat abusive, the pairs of helical flexural modes identified from their cylindrical counterparts have been denoted with superscripts + and – in this paper. It should also be noted that the flexural modes  $F(1,2)^{+-}$  are not strictly evanescent any more but inhomogeneous, unlike their cylindrical counterparts. Figure 7 gives some FE modeshapes obtained at  $\Omega=1$ .

As a side but interesting remark, Fig. 6 also allows to evaluate the high frequency limit of a Timoshenko model. For  $\Omega=2.0$ , the wavenumber differences between FE and Timoshenko models is approximately 3, 0, 5 and 9% respectively for the  $F(1,1)$ , torsional mode,  $L(0,1)$  and  $F(1,2)$  modes (for both the cylindrical and helical cases). For

instance, if a maximum dispersion error of about 2% is sought, this limit is  $\Omega_{lim}=1.4$  (for a typical cross-sectional radius  $a=2.5\text{mm}$ , it corresponds to  $f_{lim}=280\text{kHz}$ ). As expected, significant differences increase above the  $F(1,2)$  cut-on frequency and as the next upper mode (not taken into account by a Timoshenko model) is reaching its cut-on frequency.

Figure 9 gives dispersion curves for the helical case of both FE and Timoshenko models with  $\Omega$  varying from near 0 to 0.02. The agreement between both models is still perfect, as expected for this very low-frequency range. However, what physically happens must be outlined. Strong differences occur in the helical case so that a direct analogy with the cylinder becomes difficult. The torsional and  $L(0,1)$  modes are respectively cut-off near  $\Omega=0.010$  and  $0.014$  (for the cylinder, these modes are always propagative). Between  $\Omega=0.009$  and  $0.002$ , both modes have the same wavenumbers and are strongly coupled. It is then difficult to distinguish which modes shapes corresponds to a compressional or torsional behavior. Thus,  $l$  and  $t$  notations have been replaced to denote respectively compression and torsion dominant modes (but this choice may be somewhat subjective). Besides, it should be noted that these modes are still attenuated but becomes inhomogeneous (non-zero real and imaginary parts) for this frequency range. Under  $0.002$ , both modes propagate again, with different phase velocities. The  $l$  mode has a decreasing slope indicating a negative group velocity (while its phase velocity is positive). For the helical waveguide considered, it can be concluded that bandcut attenuation zones exist for the torsional and  $L(0,1)$  modes, which are

respectively about [0.002;0.010] and [0.002;0.0014] (with  $a=2.5\text{mm}$ , [400;2000] Hz and [400;2800] Hz).

Figure 10 gives  $l$  and  $t$  modeshapes computed for  $\Omega=0.0011$ . They look like each other but the mode  $t$  exhibits a slight torsional behavior, unlike the mode  $l$ .

In order to briefly examine the influence of the helix step, some computations have also been made for the lay angles  $6^\circ$  and  $9^\circ$ . As shown in Fig. 10, all the above mentioned differences between helical and cylinder geometry increase as the lay angle increases. Pairs of flexural modes become more and more distinct and the bandcut zone grows.

Then, it is also observed that there exists some rigid-body modes ( $\omega=0$ ) for wavenumbers coinciding with  $2\pi/l_0$  (see Figs. 9 and 11), i.e. an axial wavelength equal to the arc length of one helix step (this wavenumber value is also the real part of the inhomogeneous  $F(1,2)^{+/-}$  modes). This result was already reported by Tso<sup>31</sup> in 1972 when studying lower propagation modes of a helical Euler-Bernoulli beam.

Finally, in order to show the capabilities of the FE method proposed in this paper, Fig. 12 exhibits the dispersion curves of the cylinder and the helical waveguides ( $\phi=7.5^\circ$ ) for a higher frequency range, varying from 0 to 5 (which is far above the limit of Timoshenko type approximation). A rough criterion of  $\lambda_s/h=20$  at  $\Omega=5$  has been

chosen for the mesh with  $h_{axis}=0.7h$ , yielding 10456 elements and 11997 dofs (deformed mesh depicted in Fig. 13). Only modes that propagate at  $\Omega = 5$  have been plotted on the dispersion curves. At this frequency, there are three propagating compressional modes:  $L(0,1)$ ,  $L(0,2)$  and  $L(0,3)$ , represented in bold solid lines for clarity. In the cylinder case, the FE dispersion error remains less than 1% compared with the Pochhammer-Chree solutions, so that a good accuracy can be expected for the helical FE model. The comparison of results obtained with the cylindrical and helical waveguides clearly shows that the wavenumbers of compressional and torsional modes are unchanged, while those of flexural modes are different and do not occur in double roots in the helical case (though their imaginary parts seem to remain unchanged). As an illustrative example, Fig. 13 exhibits the  $L(0,2)$  modeshapes at  $\Omega = 5$ .

## V. CONCLUSION

Elastic wave propagation inside a helical waveguide has been analyzed through a three-dimensional FE method based on periodic boundary conditions and a translationally invariant mapping. This method can be implemented as a post-processing step of a conventional FE code providing stiffness, mass and damping matrices. As opposed to SAFE methods, it avoids to write equilibrium equations in a helical curvilinear coordinate system, somewhat difficult to use, as well as a complete re-programming inside a FE code. The convergence and accuracy of the proposed method have been studied, and were shown to be similar to a SAFE method. With linear prisms (triangles in a section), a criterion of about  $\lambda_s/20$  can be applied to generate the FE mesh.

From a physical point of view, the dispersion curves of a helical waveguide exhibit several differences compared with the cylinder. Wavenumbers for compression modes remain identical – provided that the arc length of the helix centerline is considered – but flexural modes does not occur in pairs of equal wavenumbers due to the lack of symmetry of the helical geometry. This difference is stronger as the lay angle increases. Besides, there exists some low-frequency bandcut zones where both the compressional and torsional modes become non-propagating. These bands grow with an increasing helix lay angle. In the low-frequency range, FE results have been verified with a helical Timoshenko beam model, which has also allowed evaluating the high frequency limit of such a model. Further studies should deal with the use of higher order finite elements and a comparison with experimental results.

## APPENDIX: HELICAL TIMOSHENKO BEAM MODEL **Equation Section 1**

Assuming a  $e^{i(ks-\omega t)}$  dependence, it can be shown that the equilibrium equations for a helical Timoshenko beam are written as follows<sup>30</sup>:

$$\left(\mathbf{A}_1 - \omega^2 \mathbf{A}_2 - ik\mathbf{B} - k^2 \mathbf{C}\right)\mathbf{u} = \mathbf{0} \quad (\text{A.1})$$

with notations:

$$\begin{aligned}
 \mathbf{A}_1 = & \begin{bmatrix} \tau_0^2 \sigma_2 + \kappa_0^2 \sigma_p & 0 & 0 & 0 & \tau_0 \sigma_2 & 0 \\ 0 & \tau_0^2 \sigma_1 & -\kappa_0 \tau_0 \sigma_1 & \tau_0 \sigma_1 & 0 & 0 \\ 0 & -\kappa_0 \tau_0 \sigma_1 & \kappa_0^2 \sigma_1 & -\kappa_0 \sigma_1 & 0 & 0 \\ 0 & \tau_0 \sigma_1 & -\kappa_0 \sigma_1 & \sigma_1 + \tau_0^2 \beta_2 & 0 & -\tau_0 \kappa_0 \beta_2 \\ \tau_0 \sigma_2 & 0 & 0 & 0 & \sigma_2 + \tau_0^2 \beta_1 + \kappa_0^2 \beta_T & 0 \\ 0 & 0 & 0 & -\tau_0 \kappa_0 \beta_2 & 0 & \kappa_0^2 \beta_2 \end{bmatrix}, \quad \mathbf{u} = \begin{Bmatrix} u \\ v \\ w \\ \theta_1 \\ \theta_2 \\ \theta_T \end{Bmatrix} \\
 \mathbf{B} = & \begin{bmatrix} 0 & -\tau_0(\sigma_1 + \sigma_2) & \kappa_0(\sigma_1 + \sigma_p) & -\sigma_1 & 0 & 0 \\ \tau_0(\sigma_1 + \sigma_2) & 0 & 0 & 0 & \sigma_2 & 0 \\ -\kappa_0(\sigma_1 + \sigma_p) & 0 & 0 & 0 & 0 & 0 \\ \sigma_1 & 0 & 0 & 0 & \tau_0(\beta_1 + \beta_2) & 0 \\ 0 & -\sigma_2 & 0 & -\tau_0(\beta_1 + \beta_2) & 0 & \kappa_0(\beta_2 + \beta_T) \\ 0 & 0 & 0 & 0 & -\kappa_0(\beta_2 + \beta_T) & 0 \end{bmatrix} \quad (\text{A.2}) \\
 \mathbf{A}_2 = & \text{diag}(m, m, m, mk_1^2, mk_2^2, mk_T^2) \quad , \quad \mathbf{C} = -\text{diag}(\sigma_1, \sigma_2, \sigma_p, \beta_1, \beta_2, \beta_T)
 \end{aligned}$$

$u, v, w$  denote the components of displacements of the centroid of the cross-section in the Frenet basis  $(\mathbf{N}, \mathbf{B}, \mathbf{T})$ .  $\theta_1, \theta_2, \theta_T$  are the components of rotation of the cross-section.  $m$  is the mass per unit length.  $\sigma_1, \sigma_2$  are the shear rigidities and  $\sigma_p$  the extensional rigidity.  $\beta_1, \beta_2$  are the flexural rigidities and  $\beta_T$  the torsional rigidity.  $k_1, k_2$  are the radii of gyration and  $k_T$  is the polar radii of gyration of the cross-section. It is assumed that the condition  $(\kappa_0 k_T)^2 \ll 1$  is satisfied, which implies that the wire curvature has a negligible effect on the various rigidities (and that the cross-sectional dimensions of the wire are small compared with the radius of curvature of the helix). For further theoretical details, the reader is referred to the paper of Wittrick [30]. For a circular cross-section of radius  $a$ , the properties are given by:



$$\begin{aligned}
m &= \rho\pi a^2, \quad \sigma_1 = \sigma_2 = \eta E\pi a^2/2(1+\nu), \quad \sigma_p = E\pi a^2, \quad \eta = 6/7, \\
\beta_1 = \beta_2 &= E\pi a^4/4, \quad \beta_T = E\pi a^4/4(1+\nu), \quad k_1 = k_2 = a/2, \quad k_T = a\sqrt{2}/2
\end{aligned} \tag{A.3}$$

Eqs. (A.1) is a quadratic eigenvalue problem. Its characteristic equation, which is a polynomial of degree twelve, was not solved by Wittrick. In this paper, the eigensystem (A.1) is solved using a standard numerical eigensolver instead.

- <sup>1</sup> B. N. Pavlakovic, M. J. S. Lowe, and P. Cawley, “High-frequency low-loss ultrasonic modes in imbedded bars,” *Journal of Applied Mechanics* **68**, 67–75 (2001).
- <sup>2</sup> P. Rizzo, and F. Lanza di Scalea, “Load Measurement and health monitoring in cable stays via guided wave magnetostrictive ultrasonics,” *Materials Evaluation* **62**, 1057–1065 (2004).
- <sup>3</sup> J. Zemanek, “An experimental and theoretical investigation of elastic wave propagation in a cylinder,” *Journal of the Acoustical Society of America* **51**, 265–283 (1972).
- <sup>4</sup> H. Kwun, K. A. Bartels, and J. J. Hanley, “Effects of tensile loading on the properties of elastic-wave propagation in a strand,” *Journal of the Acoustical Society of America* **103**, 3370–3375 (1998).
- <sup>5</sup> M. D. Beard, M. J. S. Lowe, and P. Cawley, “Ultrasonic guided waves for inspection of grouted tendons and bolts,” *Journal of Materials in Civil Engineering* **212**, 212–218 (2003).
- <sup>6</sup> P. Rizzo, and F. Lanza di Scalea, “Wave propagation in multi-wire strands by wavelet-based laser ultrasound,” *Experimental Mechanics* **44**, 407–415 (2004).
- <sup>7</sup> P. Rizzo, “Ultrasonic wave propagation in progressively loaded multi-wire strands,” *Experimental Mechanics* **46**, 297–306 (2006).

- <sup>8</sup> L. Laguerre, J.-C. Aime, M. Brissaud, “Magnetostrictive pulse-echo device for non-destructive evaluation of cylindrical steel materials using longitudinal guided waves,” *Ultrasonics* **39**, 503–514 (2002).
- <sup>9</sup> L. Gavric, “Computation of propagative waves in free rail using a finite element technique,” *Journal of Sound and Vibration* **185**, 531–543 (1995).
- <sup>10</sup> N. Rattanawangcharoen, W. Zhuang, A. H. Shah, and S. K. Datta, “Axisymmetric guided waves in jointed laminated cylinders,” *Journal of Engineering Mechanics* **123**, 1020–1026 (1997).
- <sup>11</sup> W. Zhuang, A. H. Shah, and S. B. Dong, “Elastodynamic Green’s function for laminated anisotropic circular cylinders,” *Journal of Applied Mechanics* **66**, 665–674 (1999).
- <sup>12</sup> T. Hayashi, W.-J. Song, and J. L. Rose, “Guided wave dispersion curves for a bar with an arbitrary cross-section, a rod and rail example,” *Ultrasonics* **41**, 175–183 (2003).
- <sup>13</sup> V. Damljanovic, and R. L. Weaver, “Propagating and evanescent elastic waves in cylindrical waveguides of arbitrary cross-section,” *Journal of the Acoustical Society of America* **115**, 1572–1581 (2004).
- <sup>14</sup> T. Hayashi, C. Tamayama, and M. Murase, “Wave structure of guided waves in a bar with an arbitrary cross-section,” *Ultrasonics* **44**, 17–24 (2006).
- <sup>15</sup> P. Wilcox, M. Evans, O. Diligent, M. Lowe, and P. Cawley, “Dispersion and excitability of guided acoustic waves in isotropic beams with arbitrary cross section,”

- D. Thompson and D. Chimenti (eds), American Institute of Physics, Review of Progress in Quantitative NDE **21**, 203–210 (2002).
- <sup>16</sup> A. Demma, P. Cawley, and M. Lowe, “The effect of bends on the propagation of guided waves in pipes,” *Journal of Pressure Vessel Technology* **127**, 328–335 (2005).
- <sup>17</sup> D. J. Mead, “Wave propagation in continuous periodic structures: research contributions from Southampton, 1964–1995,” *Journal of Sound and Vibration* **190**, 495–524 (1996).
- <sup>18</sup> D. J. Mead, “A general theory of harmonic wave propagation in linear periodic systems with multiple coupling,” *Journal of Sound and Vibration* **27**, 235–260 (1973).
- <sup>19</sup> A. Ghoshal, M. L. Accorsi, and M. S. Bennett, “Wave propagation in circular cylindrical shells with periodic axial curvature,” *Wave Motion* **23**, 339–352 (1996).
- <sup>20</sup> L. Gry, and C. Gontier, “Dynamic modeling of railway track: a periodic model based on a generalized beam formulation,” *Journal of Sound and Vibration* **199**, 531–558 (1997).
- <sup>21</sup> B. R. Mace, D. Duhamel, and M. J. Brennan, “Finite element prediction of wave motion in structural waveguides,” *Journal of the Acoustical Society of America* **117**, 2835–2843 (2005).
- <sup>22</sup> D. Duhamel, B. R. Mace, and M. J. Brennan, “Finite element analysis of the vibrations of waveguides and periodic structures,” *Journal of Sound and Vibration* **294**, 205–220 (2006).

- <sup>23</sup> R. S. Langley, “A variational principle for periodic structures,” *Journal of Sound and Vibration* **135**, 135–142 (1989).
- <sup>24</sup> W. X. Zhong, and F. W. Williams, “On the direct solution of wave propagation for repetitive structures,” *Journal of Sound and Vibration* **181**, 485–501 (1995).
- <sup>25</sup> W. Sollfrey, “Wave propagation on helical wires,” *Journal of Applied Physics* **22**, 905–910 (1951).
- <sup>26</sup> A. Nicolet, F. Zola, and S. Guenneau, “Modeling of twisted optical waveguides with edge elements,” *The European Physical Journal Applied Physics* **28**, 153–157 (2004).
- <sup>27</sup> T. R. Meeker, and A. H. Meitzler, “Guided wave propagation in elongated cylinders and plates,” *Physical Acoustics* (Academic, New York, 1964), Vol. 1, Sec. A2.
- <sup>28</sup> J. M. Galan, and R. Abascal, “Elastodynamic guided wave scattering in infinite plates,” *International Journal for Numerical Methods in Engineering* **58**, 1091–1118 (2003).
- <sup>29</sup> J. M. Galan, and R. Abascal, “Lamb mode conversion at edges. A hybrid boundary-element–finite-element solution,” *Journal of the Acoustical Society of America* **117**, 1777–1784 (2005).
- <sup>30</sup> W. H. Wittrick, “On elastic wave propagation in helical springs,” *International Journal of Mechanical Sciences* **8**, 25–47 (1966).
- <sup>31</sup> W. K. Tso, “On the motion of a curved and twisted rod,” *Acta Mechanica* **13**, 163–178 (1972).

TABLE I: Characteristics of meshes (in parenthesis:  $\lambda_y/h$  criterion for  $\Omega=1$ ).

No.	$h$ ( $\lambda_y/h$ )	# of elements	# of dofs
1	1 (6)	32	54
2	0.5 (12)	112	150
3	0.25 (25)	416	486
4	0.125 (50)	1600	1734

TABLE II: FE adimensional wavenumbers computed with the same cross-sectional mesh ( $\lambda_s/h=20$ ) but a varying number of layers of elements ( $\phi=45^\circ$  and  $\Omega=0.75$ ).

	1 layer	10 layers	30 layers	whole step
$L(0,1)$	0.4057	0.4057	0.4058	0.4058
torsion	0.6305	0.6305	0.6305	0.6305
$F(1,1)^-$	1.0135	1.0135	1.0135	1.0136
$F(1,1)^+$	1.4476	1.4476	1.4476	1.4476

FIGURE CAPTIONS:

FIG.1: Example of a non-uniform periodic waveguide with its unit periodic cell and boundaries notations.

FIG.2: Meshes 1 to 4, with successive refinements.

FIG.3: Dispersion error with respect to the Pochhammer-Chree solution (subscript  $p$ ) vs.  $1/h$  at  $\Omega=1$  for the first propagating, evanescent and inhomogeneous modes. As a reference, the dotted line is the quadratic rate  $(1/h)^2$ .

FIG.4: Dispersion error at  $\Omega=1$  vs.  $h/h_{axis}$ , obtained by reducing the axial element length (same legend as in Fig. 1). The cross-section mesh of mesh 2 is taken ( $\lambda_s/h=10$ ).

FIG.5: Meshes of the helical waveguide ( $\phi=45^\circ$ ) with only one layer of elements and for the whole helix step (60 layers).

FIG.6: Dispersion curves for the first six propagating modes for  $\Omega$  ranging from 0.02 to 2 ( $\phi=7.5^\circ$ ). Left: cylinder, right: helical. Solid lines: FE model, dashed lines: Timoshenko beam model.



FIG.7: (a) undeformed FE mesh used for the helical waveguide for computations between  $\Omega=0$  and 2, (b)  $F(1,1)^+$ , (c)  $F(1,1)^-$ , (d) torsional and (e)  $L(0,1)$  modeshapes (displacement real part, with deformed mesh) computed for  $\Omega=1$ .

FIG.8: Dispersion error with respect to the reference solution ( $\lambda_s/50$  mesh) vs.  $1/h$  at  $\Omega=2$  for the six modes (dotted line: quadratic rate).

FIG.9: Dispersion curves of the helical waveguide ( $\phi=7.5^\circ$ ) with  $\Omega$  varying from 0 to 0.02. Solid lines: FE model, dashed lines: Timoshenko beam model (gray lines: cylinder).  $\bullet$ : cut-off frequencies,  $\circ$ : rigid-body modes.

FIG.10: Real part of displacement for modeshapes  $t$  (left) and  $l$  (right) computed for  $\Omega=0.0011$ .

FIG.11: Dispersion curves of the helical waveguide (FE model only) with  $\Omega$  varying: from 0.02 to 2 (left) and from 0 to 0.02 (right). Solid lines:  $\phi=9.0^\circ$ , dashed lines:  $\phi=6.0^\circ$ , gray lines: cylinder  $\phi=0^\circ$ .

FIG.12: FE Dispersion curves of cylindrical (up) and helical  $\phi=7.5^\circ$  (bottom) waveguides. Bold lines: compressional modes ( $L(0,1)$ ,  $L(0,2)$  and  $L(0,3)$ ), gray line: torsional mode, thin lines: flexural modes. Lines are dotted when modes are non-propagating (evanescent or inhomogeneous).

FIG.13: Real part of displacement for the  $L(0,2)$  modeshapes computed for  $\Omega=5$  for the cylinder (left) and the helical waveguide (right).

FIG.1

Fabien Treyssède

JASA

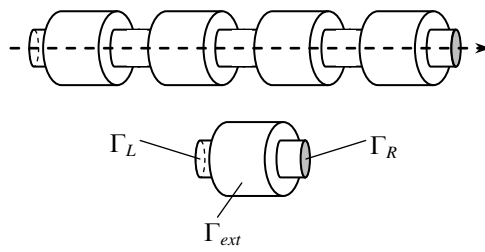


FIG.2

Fabien Treyssède

JASA

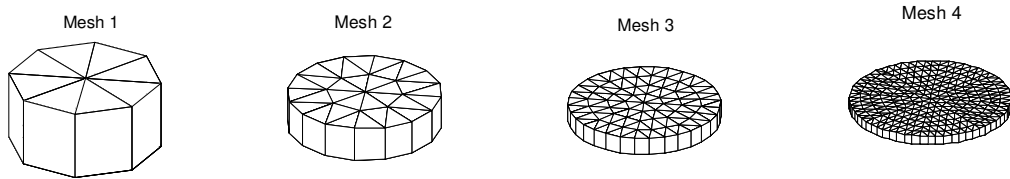


FIG.3

Fabien Treyssède

JASA

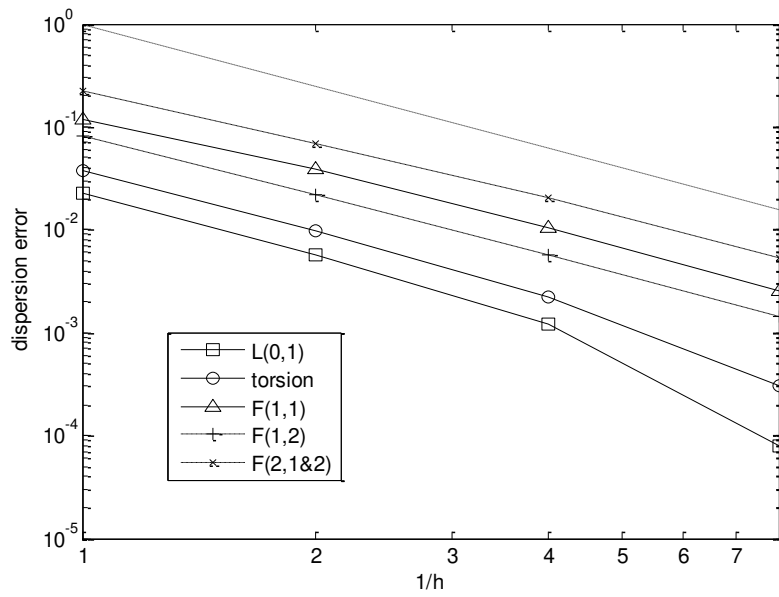


FIG.4  
Fabien Treyssède  
JASA

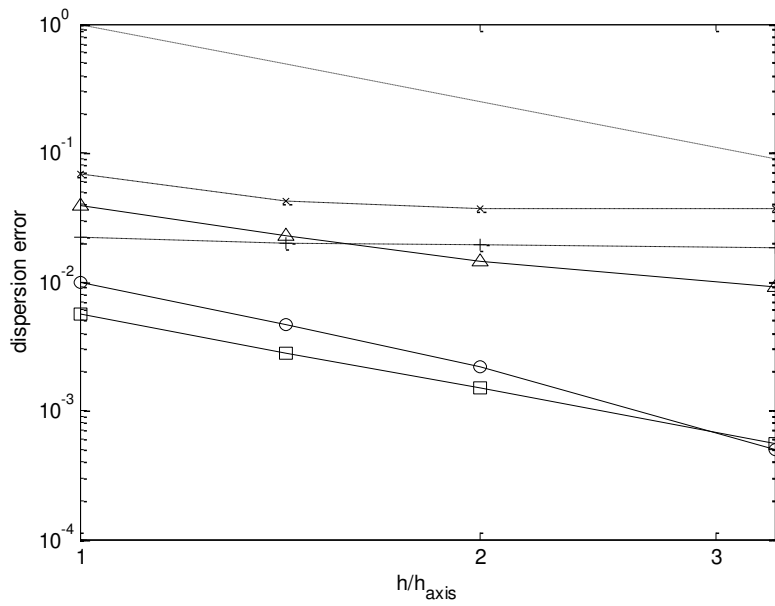


FIG.5

Fabien Treyssède

JASA

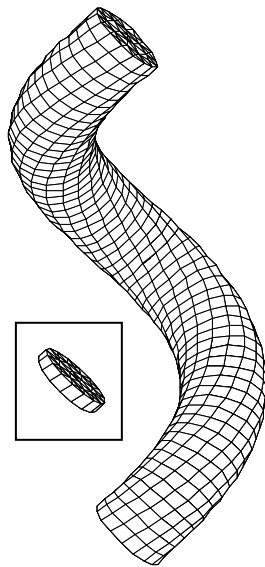


FIG.6

Fabien Treyssède

JASA

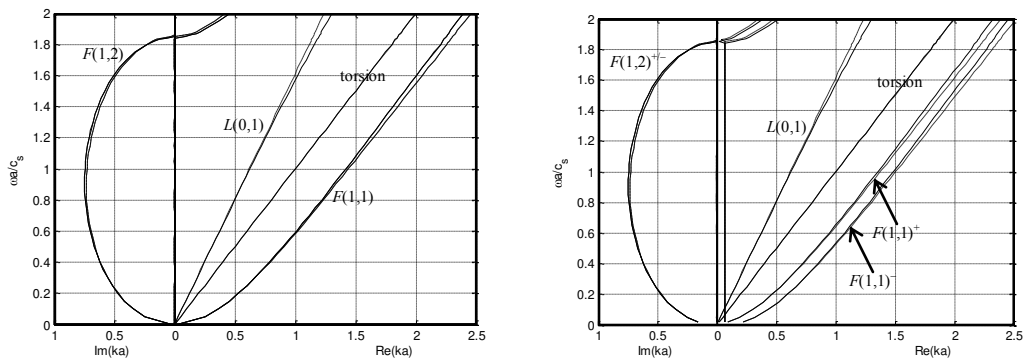




FIG.7  
Fabien Treyssède  
JASA

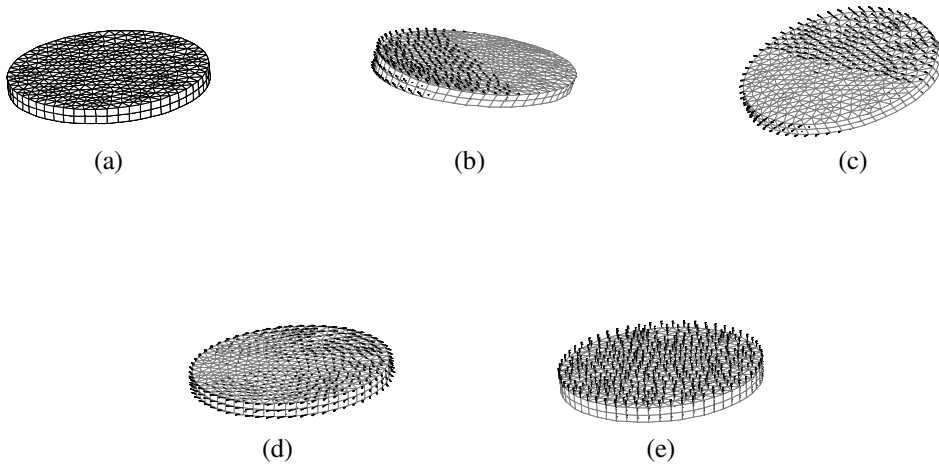


FIG.8

Fabien Treyssède

JASA

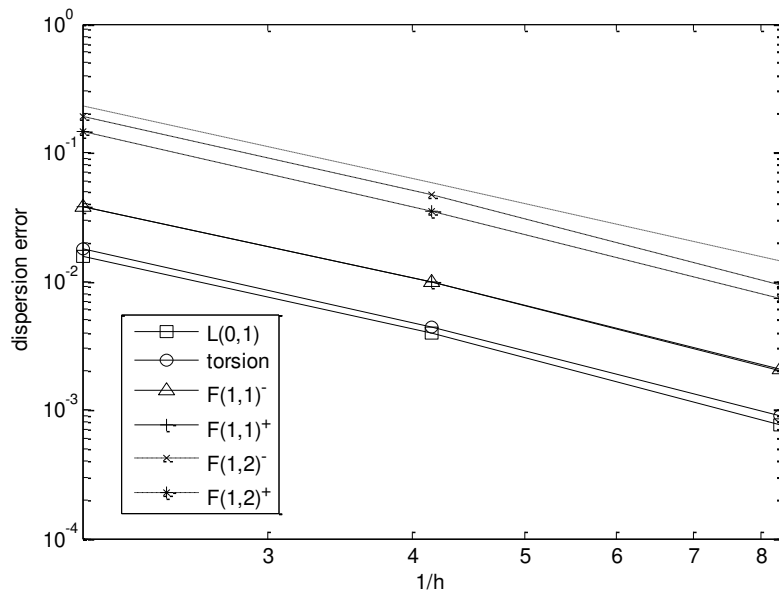


FIG.9

Fabien Treyssède

JASA

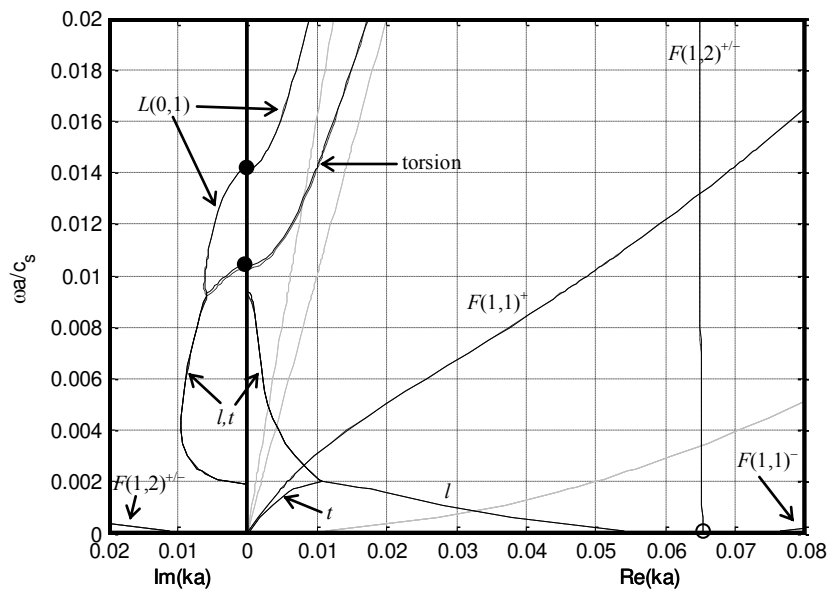


FIG.10

Fabien Treyssède

JASA



FIG.11

Fabien Treyssède

JASA

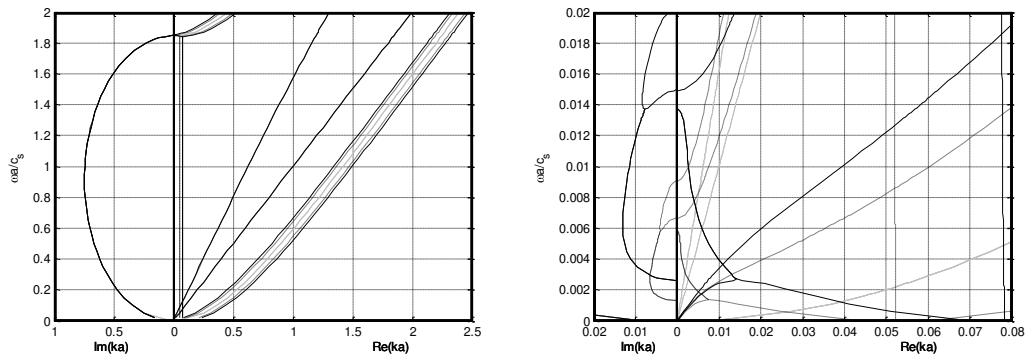


FIG.12

Fabien Treyssède

JASA

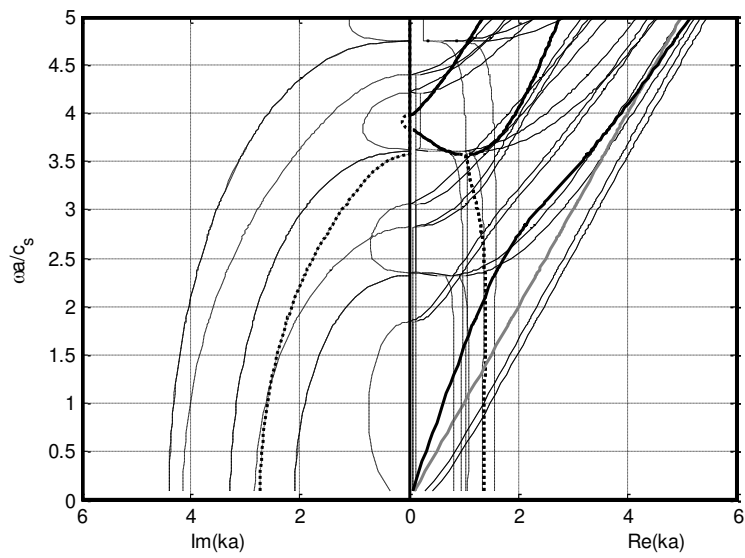
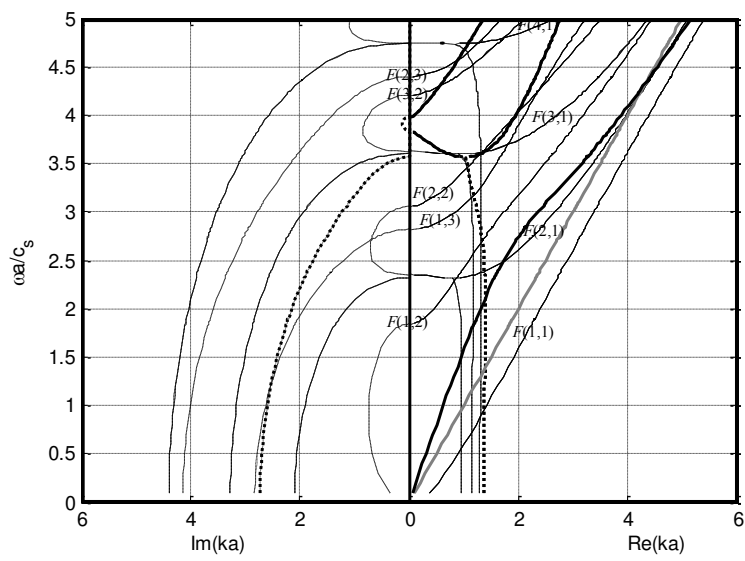


FIG.13

Fabien Treyssède

JASA

